RSC Advances

RSC Publishing

PAPER

View Article Online
View Journal | View Issue

Cite this: *RSC Adv.*, 2013, **3**, 23638

Facile preparation, high microwave absorption and microwave absorbing mechanism of RGO–Fe_3O_4 composites†

Meng Zong, Ying Huang,* Yang Zhao, Xu Sun, Chunhao Qu, Didi Luo and Jiangbo Zheng

Reduced graphene oxide (RGO)–Fe_3O_4 composites with obviously enhanced microwave absorption properties were successfully fabricated by a rational one-pot simplified co-precipitation route, which avoided the usage of an inert gas and any additional chemical agents (such as surfactants and stabilizers). Given these advantages, the strategy described in this study can be developed as a simple and large-scale route to yield RGO–Fe_3O_4 composites. The morphology, structure, thermal stability, magnetic and microwave electromagnetic properties of the as-prepared composites were characterized by XRD, XPS, TEM, FT-IR, Raman, TG and VSM. These composites exhibit excellent microwave absorption properties, which are attributed to effective complementarities between the dielectric loss and the magnetic loss. The microwave absorption mechanism of the RGO–Fe_3O_4 composites was studied in detail. For the RGO–Fe_3O_4-3 composite, the maximum R_L reaches −44.6 dB at 6.6 GHz with a thickness of 3.9 mm, and the bandwidth of R_L less than −10 dB can reach up to 4.3 GHz (from 12.2 to 16.5 GHz) with a thickness of 2.0 mm. Moreover, the microwave absorption properties can be tuned easily by varying the (RGO)/(Fe_3O_4) ratio and layer thickness of the samples. It is believed that such composites will find wide applications in the microwave absorbing area.

Received 2nd July 2013
Accepted 9th September 2013

DOI: 10.1039/c3ra43359e

www.rsc.org/advances

1. Introduction

With the development of electronic technology, electromagnetic (EM) interference has become a pollution problem, not only influencing the operation of electronic devices, but also being harmful to the health of human beings.[1,2] Microwave absorbing materials have attracted much attention owing to these expanding EM interference problems.[3–5] They can absorb microwaves effectively and convert EM energy into thermal energy or dissipate microwaves by interference. Microwave absorbing materials are now required to have strong absorption characteristics, wide absorption frequencies, be lightweight and have antioxidation properties.[4] There are a number of microwave absorbing materials such as ferrites, carbonyl iron, conducting polymers and carbon-based materials *etc.*[6–9] However, the traditional microwave absorbing materials cannot meet all of the requirements such as to be strong, wide, lightweight and thin at the same time. Hence, extensive studies have been made to develop novel microwave absorbing materials with high absorption and wide absorption frequencies.

Graphene, a novel carbon nanomaterial consisting of one-atom-thick, hexagonally arranged carbon atoms, has attracted extensive attention owing to its superior electronic, thermal and mechanical properties as well as its chemical stability.[10,11] Due to its special surface properties and layered structure, graphene has become a potential nanoscale building block for new hybrid materials.[12] Recent research shows that inorganic nanoparticles, such as Au, Ag, Fe_3O_4 and Co_3O_4, *etc.*, could be attached to graphene or graphene oxide (GO) to form hybrid materials, which have potential applications in surface enhanced Raman scattering (SERS), lithium ion batteries, hydrogen storage, microwave absorption and as a magnetic resonance imaging (MRI) contrast agent, *etc.*[13–16]

As a class of promising microwave absorbing materials, carbon-based materials exhibited several exceptional properties including being lightweight, having wide absorption frequency, high thermal stability, and high chemical stability.[1] In previous research, Zhan and co-workers[17,18] did some work on the synthesis of the heterojunction of Fe_3O_4 with carbon nanotubes (CNTs) or graphene, revealing that hybrid materials can reinforce the original properties and extend the applications of simplex materials. In comparison with CNTs, graphene possesses similar physical properties but has larger surface areas, a lower price and more stable properties. Furthermore,

Department of Applied Chemistry, The Key Laboratory of Space Applied Physics and Chemistry, Ministry of Education, School of Science, Northwestern Polytechnical University, Xi'an 710072, PR China. E-mail: nwpu_zongmeng@163.com; yingh@nwpu.edu.cn; Tel: +86 29 88431636

† Electronic supplementary information (ESI) available. See DOI: 10.1039/c3ra43359e

more effective absorption could be obtained by platelet-shaped materials than by the rod-shaped and sphere-shaped ones in microwave absorption applications.[17] Therefore, graphene is highly expected to be the alternative to CNTs in microwave absorbing materials.

As is known, Fe_3O_4 has an inverse spinel structure, in which half of the Fe^{3+} cations occupy tetrahedral (A) sites, while all of the Fe^{2+} cations and the other half of the Fe^{3+} cations occupy octahedral (B) sites, resulting in the structural formula of $Fe^{3+}{}_AFe^{3+}Fe^{2+}{}_BO_4$.[19] It is an important magnetic material and has physical and chemical properties such as superparamagnetism, half-metallic character and strong spin polarization at room temperature in addition to its low toxicity and high biocompatibility. Moreover, its magnetic properties can be tuned by size, shape, and dimension.[4] Thus, Fe_3O_4 has wide applications in many areas such as gas sensors, magnetic storage media, optoelectronic and spintronic devices, biomedicine, as well as materials for microwave absorbing and shielding research.[4,20–22] However, its heavy weight restrain it from being widely used in the field of electromagnetic wave absorption.[23] Furthermore, its microwave absorption properties are usually subject to the degradation caused by the eddy current in the high-frequency region.[4]

Herein, the reduced graphene oxide (RGO) coated with Fe_3O_4 nanoparticles (NPs) was synthesized through a facile one-pot simplified co-precipitation method, which avoided the usage of an inert gas or any additional surfactants or stabilizers. The strategy described in this study can be developed as a simple and large-scale route to yield RGO–Fe_3O_4 composites. The crystalline structure, morphology, thermal stability, magnetic properties and microwave electromagnetic properties of the as-prepared composites were investigated. The mechanism of the enhanced reflection loss for the RGO–Fe_3O_4 composites will also be explained comprehensively.

2. Experimental method

2.1 Preparation of RGO–Fe_3O_4 composites

GO was prepared by Hummers' method as reported in ref. 24. The composites of RGO–Fe_3O_4 were prepared by a one-pot simplified co-precipitation route. In a typical procedure, 100 mg GO was dispersed in 150 mL of deionized water and ultrasonicated for 2 h. 88 mg $FeCl_3\cdot 6H_2O$ and 65 mg $FeCl_2\cdot 4H_2O$ (Fe^{3+} and Fe^{2+} with a mole ratio of 1 : 1) were dispersed in 50 mL deionized water and were then added to the suspension of GO. 1 M NaOH aqueous solution was added to the suspension until the pH = 11, and the mixture was stirred for 2 h at 80 °C without protection of an inert gas. Subsequently, a freshly prepared $NaBH_4$ aqueous solution ($NaBH_4$ and GO with a mass ratio of 6 : 1) was added dropwise with stirring and the mixture was stirred again for 1 h at 80 °C to ensure complete reduction of GO. The black products were washed several times with deionized water and ethanol, then dried at 60 °C under vacuum and denoted as RGO–Fe_3O_4-1. With different weights of GO (50 mg, 25 mg, 0 mg) being added to the reaction system, the final samples were labeled as RGO–Fe_3O_4-2, RGO–Fe_3O_4-3, and Fe_3O_4, respectively. For comparison purposes, RGO was also prepared in similar procedures in the absence of Fe^{3+}, Fe^{2+} and NaOH.

2.2 Characterization

The crystal structure was determined by X-ray diffraction (XRD, Rigaku, model D/max-2500 system at 40 kV and 100 mA of Cu Kα). XPS analysis was characterized by an X-ray photoelectron spectrometer (K-Alpha; Thermo Fisher Scientific (SID-Elemental), New York, USA). The morphology and the size of the synthesized samples were characterized by transmission electron microscopy (TEM, Tecnai F30 G2, FEI, USA). The Fourier transform infrared spectroscopy (FT-IR) spectra of the composites were obtained by using a Model NIcolETiS10 Fourier transform spectrometer (Thermo SCIENTIFIC Co., USA) with a 2 cm^{-1} resolution in the range of 4000–400 cm^{-1}. The Raman spectra of the composites were obtained by using an in Via Laser Raman spectrometer (Renishaw Co., England) with 514 nm radiation. The thermal stabilities of the composites were analyzed by using thermogravimetric analysis (TGA, Model Q50, TA, USA) from room temperature to 800 °C in an air atmosphere, with a heating rate of 20 °C min^{-1}. The magnetic properties were measured by a vibrating sample magnetometer (VSM, Riken Denshi, BHV-525) at room temperature. Electromagnetic (EM) parameters were measured by a vector network analyzer (NA, HP8720ES) in the range of 2–18 GHz, in which the synthesized powders were pressed to be toroidal samples (outer diameter: 7 mm, inner diameter: 3.04 mm, and thickness: 3 mm) according to the mass ratio 1 : 1 of paraffin to RGO–Fe_3O_4 composite.

3. Results and discussions

The formation of the RGO, Fe_3O_4 NPs and RGO–Fe_3O_4 composites is described in Fig. S1 (please refer to ESI†). The graphite was treated with H_2SO_4 and $KMnO_4$ and GO was obtained which contained a variety of functional groups including –COOH, –OH, epoxy and ketone.[17,25] Co-precipitation is a common method to synthesize RGO–Fe_3O_4 composites. This method always uses an inert gas (such as N_2 or Ar) to prevent the oxidation of Fe^{2+} by O_2 when Fe^{2+} : Fe^{3+} is 1 : 2.[25] In order to avoid the usage of an inert gas, we increased the ratio of the Fe^{2+}. In our work, Fe^{3+} and Fe^{2+} were dispersed in a suspension of GO with a molar ratio of 1 : 1 and adsorbed onto the surface of the GO by an electrostatic attraction. Part of the Fe^{2+} cations were oxidized by O_2 and GO.[26] Then the iron ions were transformed into Fe_3O_4 NPs on the surface of the GO by addition of NaOH at elevated temperatures. Therefore, there may be a C–O–Fe bond between the RGO and Fe_3O_4 (Fig. S2†). Finally the GO–Fe_3O_4 was reduced to RGO–Fe_3O_4 composites by $NaBH_4$. The overall reaction can be described by the following equations:

$$Fe^{2+} - e \xrightarrow{O_2,\ GO} Fe^{3+} \quad (1)$$

$$2Fe^{3+} + Fe^{2+} + 8OH^- + GO \xrightarrow{80\ ^\circ C,\ 2\ h} GO - Fe_3O_4 + 4H_2O \quad (2)$$

$$GO - Fe_3O_4 \xrightarrow{NaBH_4,\ 80\ ^\circ C,1\ h} RGO - Fe_3O_4 \quad (3)$$

The morphologies and structures of the RGO and RGO–Fe_3O_4 composites were investigated by transmission electron microscopy (TEM), which is shown in Fig. 1 and S1.† Fig. 1a and the inset in Fig. 1a show the low and high magnification TEM image of RGO, respectively, and we can see that the RGO nanosheets are less than 3 nm thick. The RGO sheets from the reduction by $NaBH_4$ of GO are transparent thin films (Fig. S1b†), and comparing with GO (Fig. S1a†), the RGO sheets have a crumpled and rippled structure which is due to deformation during the exfoliation and restacking process. Fig. 1b–d and S1c–e† show the low magnification TEM images of the obtained RGO–Fe_3O_4 composites with different (RGO)/(Fe_3O_4) ratios. It is clear that the RGO nanosheets are well loaded by Fe_3O_4 NPs, and the diameters of the Fe_3O_4 NPs are 15–25 nm. The mass ratio of (RGO)/(Fe_3O_4) has an important effect on the loading density of the Fe_3O_4 NPs on the RGO sheets. As shown in Fig. 1b–d, the densities of the Fe_3O_4 NPs increase gradually with the decrease of the GO amount used. This result is due to the fact that less GO will take up comparatively more Fe^{3+} ions to nucleate, thus leading to the increase in density of Fe_3O_4 NPs. Therefore, the amount of GO can effectively tune the density of the Fe_3O_4 NPs.[23] Moreover, almost no Fe_3O_4 NPs are found outside of the RGO nanosheets, indicating that the simplified co-precipitation synthesis of RGO–Fe_3O_4 composites has a high efficiency. The HRTEM image shown in Fig. 1e also reveals the crystalline structure of the Fe_3O_4 NPs, and the lattice fringes with interplanar distances of 0.258 nm can be assigned to the (311) planes of the cubic spinel crystal Fe_3O_4. The selected-area electron diffraction pattern (SAED) (Fig. 1f) clearly shows a ring pattern arising from the cubic spinel crystal Fe_3O_4, further confirming the crystalline nature of the Fe_3O_4 NPs.[27]

Powder X-ray diffraction (XRD) measurements were utilized to investigate the phase composition and the crystalline structure of the synthesized samples. As shown in Fig. 2a, the XRD pattern of GO shows a sharp peak at $2\theta = 11.1^\circ$, corresponding to the (001) reflection of GO. The diffraction peak of the as-prepared RGO (Fig. 2b) at 25.6° could be attributed to the graphitic structure (002) of the short-range order in stacked graphene sheets.[28] After surface decoration (Fig. 2c–e), six new peaks are observed, which are very similar to that of the pure Fe_3O_4 NPs (Fig. 2f), and could be indexed as the characteristic (220), (311), (400), (422), (511) and (440) reflections of the pure cubic spinel crystal structure of Fe_3O_4 (JCPDS no. 19-0629).[29] It can be seen that except for the peaks assigned to Fe_3O_4, no other diffraction peaks resulting from GO or graphene can be found, which indicates that the GO is effectively reduced into graphene and the self-restacking of the as-reduced graphene sheets is effectively prevented.[13] In fact, a similar result is also obtained and reported in ref. 16, 23 and 30. No peaks corresponding to impurities are detected, therefore a RGO–Fe_3O_4 heterostructure has been formed *via* a simplified co-precipitation method.

The XRD patterns of magnetite Fe_3O_4 (JCPDS no. 19-0629) and maghemite γ-Fe_2O_3 (JCPDS no. 39-1346) are highly similar, so X-ray photoelectron spectroscopy (XPS) measurements have to be consulted to unambiguously assign the crystal phase

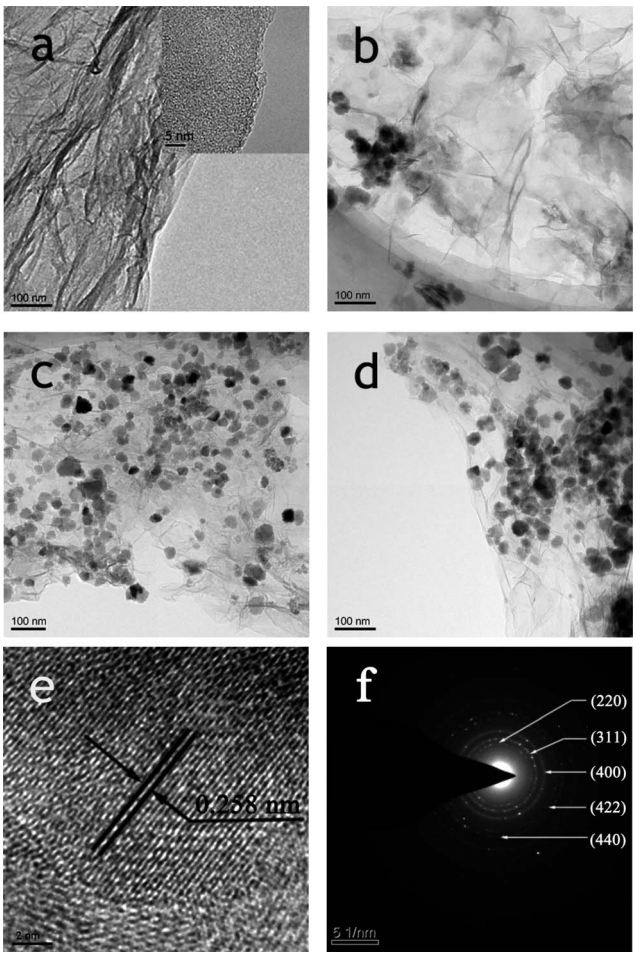

Fig. 1 TEM images of RGO (a), RGO–Fe_3O_4-1 composite (b), RGO–Fe_3O_4-2 composite (c), RGO–Fe_3O_4-3 composite (d); HRTEM image (e) and SAED pattern (f) of RGO–Fe_3O_4-2 composite.

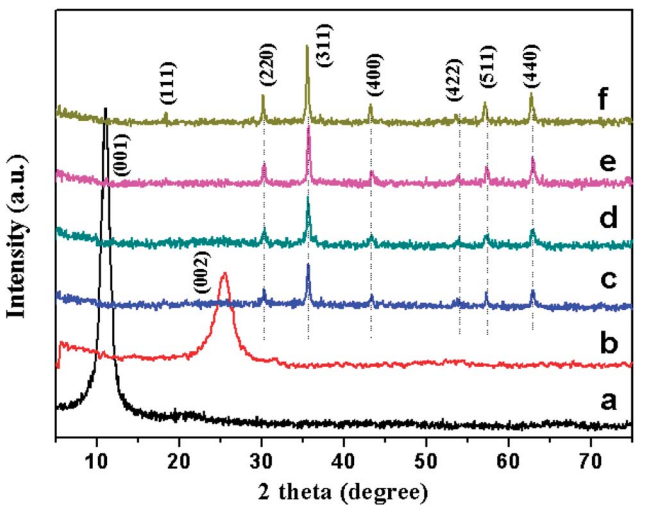

Fig. 2 XRD patterns of GO (a), RGO (b), RGO–Fe_3O_4-1 composite (c), RGO–Fe_3O_4-2 composite (d), RGO–Fe_3O_4-3 composite (e) and Fe_3O_4 NPs (f).

because XPS is very sensitive to Fe^{2+} and Fe^{3+} cations.[23,31] Since we have adopted the same synthesis process for all composites, XPS was recorded only for Fe_3O_4–RGO-1 as a representative and compared with that of GO.

Fig. 3a shows the wide scan spectrum of GO and the RGO–Fe_3O_4-1 composite. The bands observed in the wide scan XPS spectrum of RGO–Fe_3O_4-1 confirm the presence of C 1s, O 1s, and Fe 2p. The observed O 1s peak in GO at 533.1 eV is shifted to a lower binding energy (531.4 eV) due to the attachment of the Fe_3O_4 NPs in the Fe_3O_4–RGO composites.[16] As shown in Fig. 3b, the peaks located at 712.9 eV and 725.3 eV correspond to Fe $2p_{3/2}$ and Fe $2p_{1/2}$, respectively,[32] and there are no satellites for γ-Fe_2O_3 identified, excluding the presence of γ-Fe_2O_3 in the Fe_3O_4 samples,[31] which confirms that the oxide in the sample is magnetite Fe_3O_4. The C 1s spectrum of GO (Fig. 3c) and the Fe_3O_4–RGO-1 composite (Fig. 3d) consist of four main components, arising from C=C/C–C (284.6 eV) in the aromatic rings, C–O (286.4 eV) of epoxy and alkoxy, C=O (287.8 eV) and O–C=O (289.3 eV) groups.[33] After reduction, it is clear that the C/O ratio in the RGO–Fe_3O_4-1 composite increases remarkably compared with that of GO, and that most of the epoxide and hydroxyl functional groups are successfully removed, as shown in Fig. 3a, c and d. Such a higher O/C ratio of the RGO–Fe_3O_4-1 composite implies good electronic conductivity, which may enable the GO sheets to serve as conductive channels between the Fe_3O_4 NPs, and is favorable for microwave absorbing.

Fourier transform infrared spectroscopy (FT-IR) was used to indicate the degree of removal of the oxygen-containing

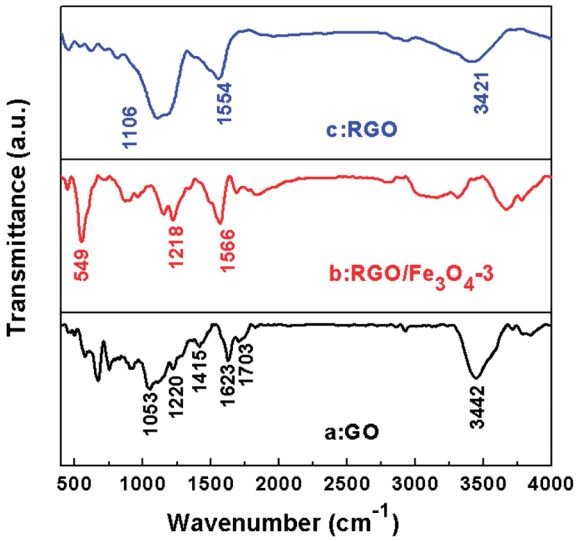

Fig. 4 FT-IR spectra of GO (a), the RGO–Fe_3O_4-3 composite (b) and RGO (c).

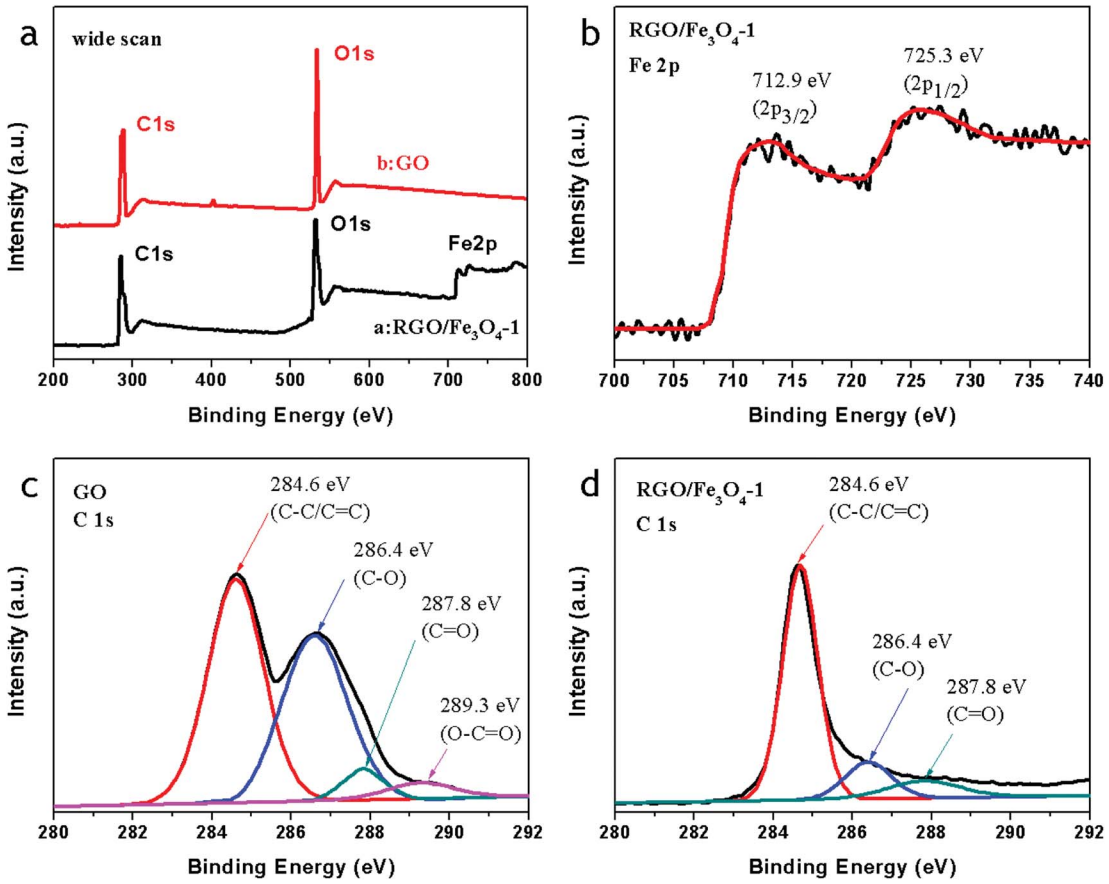

Fig. 3 X-ray photoelectron spectroscopy (XPS) spectra: wide scan (a), Fe 2p spectrum of the RGO–Fe_3O_4-1 composite (b), C 1s spectrum of RGO (c), and C 1s spectrum of the RGO–Fe_3O_4-1 composite (d).

functional groups. Fig. 4 shows the FT-IR transmittance spectra of GO (a), the RGO–Fe_3O_4-3 composite (b), and RGO (c). The spectra are shifted downward for easy viewing. The observed representative peaks in GO confirm the presence of the oxygen-containing functional groups in the carbon frameworks, which include bands at ~1057 cm^{-1} (C–O stretching vibration), ~1220 cm^{-1} (C–O stretching vibration of epoxide), ~1415 cm^{-1} (O–H stretching vibration of carboxyl), ~1703 cm^{-1} (C═O stretching of carbonyl and carboxyl groups at edges of the GO networks), while the band at ~3420 cm^{-1} could be due to the O–H stretching mode of intercalated water.[27,34–37] The band at ~1623 cm^{-1} is assigned to skeletal vibrations of the unoxidized graphitic domains.[16,27] All the absorption bands related to the oxygen-containing functional groups almost vanish in the RGO–Fe_3O_4-3 composite (Fig. 4b) and RGO (Fig. 4c), revealing that these oxygen-containing functional groups are removed in the presence of $NaBH_4$, and accordingly the GO is reduced into graphene. The band at *ca.* 1560 cm^{-1} in Fig. 4b and c could be ascribed to the formation of $-COO^-$ after coating with the Fe_3O_4 NPs.[16] Moreover, an additional peak at *ca.* 549 cm^{-1} in Fig. 4c can be ascribed to the lattice absorption of Fe_3O_4, further confirming the existence of Fe_3O_4 NPs.[27]

Raman spectroscopy is a powerful nondestructive tool to distinguish ordered and disordered crystal structures of carbon.[34] Fig. 5 shows the Raman spectra of GO, RGO and the RGO–Fe_3O_4 composites. For the GO, graphene and graphene composites, there are always two peaks appearing at about 1340 cm^{-1} and 1590 cm^{-1}, which are known as the D-band and G-band.[38] The D band is a first-order zone boundary phonon mode associated with defects in the graphene or graphene edge, while the G band is a radial C–C stretching mode of sp^2 bonded carbon.[34,39] A weak D band indicates a low density of defects and the intensity ratio of D band to G band (I_D/I_G) reflects the degree of the defects in the graphene or the edges.[39] Compared with GO, the ratio of intensities (I_D/I_G) for the RGO–Fe_3O_4 composites shows a remarkable increase, and the G band of the RGO–Fe_3O_4 composites becomes weaker and broader, suggesting a higher degree of defects in the graphene or the edges due to the reduction of $NaBH_4$ and introduction of the Fe_3O_4 NPs.[40] The defects play an important role in microwave absorbing,[41] and will further the interpretation of the microwave absorbing mechanism.

We have also examined the thermal stability of the prepared GO, RGO and RGO–Fe_3O_4 composites using thermogravimetry analysis (TGA). Thermal stability is an important material property of microwave absorption materials. Fig. 6 shows the TG analysis of GO, RGO and the RGO–Fe_3O_4 composites in an air atmosphere at a heating rate of 20 °C min^{-1}.

As shown in Fig. 6, the GO exhibits about 10 wt% loss below 100 °C and more than 41 wt% loss at 240 °C, resulting from the removal of the labile oxygen-containing functional groups such as CO, CO_2, and H_2O.[37,42] It shows a 5 wt% loss in an air atmosphere at 240 °C for the RGO, which is much lower than that of the GO, indicating a decreased amount of oxygenated functional groups. A significant drop in mass of RGO around 600 °C is due to the bulk pyrolysis of the carbon skeleton, which is similar to the drop in mass of GO around 550 °C. Thus, from the above analysis, the removal of the thermally labile oxygen functional groups by chemical reduction increased the thermal stability of graphene.[37]

From the TG curves, we can see that the RGO–Fe_3O_4 composites display three weight loss processes.[30] The slight mass loss below 100 °C is attributed to the evaporation of absorbed water. Then, a gradual weight loss occurs from 100 °C to 350 °C, which can be assigned to the removal of the labile oxygen-containing functional groups and H_2O vapor from the sample caused by the destruction of oxygenated functional groups. Next a significant weight loss occurs between 350 °C and 510 °C, indicating the oxidation and decomposition of graphene in air, leaving the final product as Fe_2O_3.[30] The skeleton of the graphene in the RGO–Fe_3O_4 composites decomposes at a lower temperature (350–510 °C) compared to that of the RGO (480–620 °C), which might be caused by the reaction of the skeleton carbon atoms and the iron oxide nanoparticles.[43]

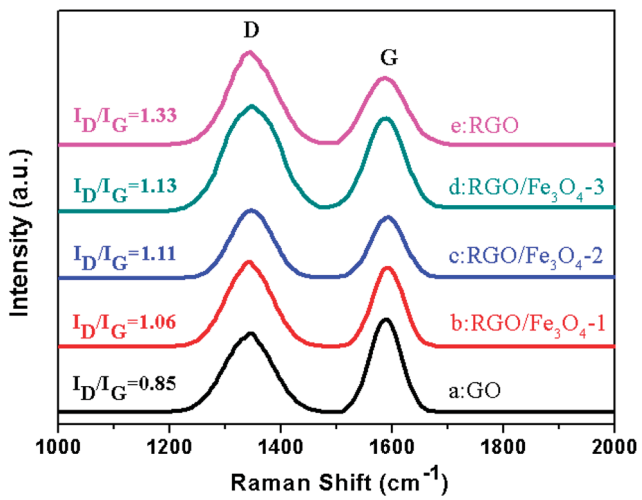

Fig. 5 Raman spectra for GO, RGO and RGO–Fe_3O_4 composites.

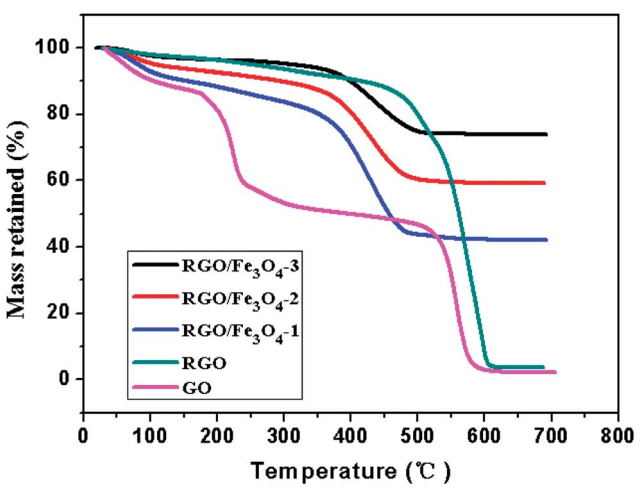

Fig. 6 TG curves of GO, RGO and RGO–Fe_3O_4 composites in air atmosphere.

The field dependence of magnetization for the Fe_3O_4 NPs and RGO–Fe_3O_4 composites was measured by a vibrating sample magnetometer (VSM) at room temperature, as shown in Fig. 7. The magnetic parameters corresponding to Fig. 7 are also shown in Table 1, including the saturation magnetization (M_s), coercivity (H_c), and remnant magnetization (M_r). It clearly shows that the M_s and M_r of the composites are increased while the H_c decreases with the increase of the Fe_3O_4 loading amount. The magnetization hysteresis loops of the Fe_3O_4 NPs and RGO–Fe_3O_4 composites are S-like, which is typical of a superparamagnetic material because of their high M_s and M_r, and low H_c,[30] implying that there is no remaining magnetization when the applied magnetic field is removed.[44] The superparamagnetic properties of the composites further confirm that the oxide in the present investigation is Fe_3O_4 rather than γ-Fe_2O_3 and is supported by the XPS spectra for Fe 2p.[38] These composites could be separated from their dispersion within 15 seconds by holding the samples close to a magnet as shown in Fig. S3,† indicating that it is possible to manipulate these composites by an external magnetic field. Additionally, the M_s value of all the RGO–Fe_3O_4 composites is lower than that of the pure bulk Fe_3O_4, which can be attributed to the nanoscale size of the Fe_3O_4 NPs and the presence of RGO.[23,44]

The electromagnetic parameters (relative complex permittivity, $\varepsilon_r = \varepsilon' - j\varepsilon''$, and relative complex permeability, $\mu_r = \mu' - j\mu''$) of the wax composites containing 50 wt% of the samples were measured at room temperature for the investigation of microwave absorption properties of the Fe_3O_4 NPs and RGO–Fe_3O_4 composites, and are shown in Fig. 8a–d. The real permittivity (ε') and real permeability (μ') symbolize the storage ability of electric and magnetic energy, while the imaginary permittivity (ε'') and imaginary permeability (μ'') are related to the dissipation of electric and magnetic energy.[20]

As shown in Fig. 8a, for the RGO–Fe_3O_4-1 composite, RGO–Fe_3O_4-2 composite and RGO–Fe_3O_4-3 composite, the values of ε' are in the range of 15.37–8.22, 12.30–7.89, and 11.30–7.89, respectively, in the frequency of 2–18 GHz, and are higher than the pure Fe_3O_4 NPs (in the range of 5.04–3.13). Meanwhile, for the RGO–Fe_3O_4-1 composite, RGO–Fe_3O_4-2 composite and RGO–Fe_3O_4-3 composite, the values of ε'' are in the range of 7.67–0.88, 4.61–0.49, and 4.20–0.09, respectively, and are also higher than the pure Fe_3O_4 NPs (in the range of 1.21–0.10), as presented in Fig. 8b. It is observed that the samples with higher (RGO)/(Fe_3O_4) ratios show higher values of ε' and ε'', which is related to higher conductivities. This is because more RGO sheets increase the electric polarization and electric conductivity, since ε_r is an expression of the polarizability of a material, which consists of dipolar polarization and electric polarization at microwave frequencies.[1]

From Fig. 8c, for the RGO–Fe_3O_4-1 composite, RGO–Fe_3O_4-2 composite and RGO–Fe_3O_4-3 composite, we can see that the values of μ' are in the range of 1.18–0.83, 1.13–0.77, and 1.15–0.73, respectively, and thus have a very serious fluctuation in the 2–18 GHz frequency range. In addition, the values of μ'' for the RGO–Fe_3O_4-1 composite, RGO–Fe_3O_4-2 composite and RGO–Fe_3O_4-3 composite, as presented in Fig. 8d, are in the range of 0.87–0.03, 0.87–0.01, and 0.80 to (−0.13) in the frequency of 2–18 GHz, which are almost equal to the pure Fe_3O_4 NPs. Meanwhile, the μ'' for the RGO–Fe_3O_4 composites exhibits a broad resonance peak at 12.4–15.6 GHz with a maximum value at 14.8 GHz.

We have also calculated both the dielectric tangent loss ($\tan\delta_E = \varepsilon''/\varepsilon'$) and the magnetic tangent loss ($\tan\delta_M = \mu''/\mu'$) of the Fe_3O_4 NPs and RGO–Fe_3O_4 composites based on the permeability and permittivity of samples measured as above, shown in Fig. 8e and f. The values of $\tan\delta_E$ are mostly larger than 0.2 between 2 to 18 GHz, indicating that the dielectric loss occurs over the whole frequency range. These results suggest the RGO–Fe_3O_4 composites have distinct dielectric loss properties.

So far, there is no evidence to support the C–O–Fe bond affect on the microwave absorption properties. But the introduction of Fe_3O_4 NPs significantly enhanced the microwave absorption performance of the composites. In terms of electromagnetic theory, the dielectric loss of the RGO–Fe_3O_4 composites may be attributed to natural resonance, Debye dipolar relaxation, electron polarization relaxation and the unique layered nanostructures *etc.*[1,5,45] First, the presence of the Fe_3O_4 NPs and residual defects and groups in RGO (discussed in the Raman analysis) does not significantly alter the graphene lamellar structure, but they can act as polarized centers, which are in favor of the electromagnetic energy absorption.[1] Second, the huge aspect ratio, layered structure and high conductivity of the RGO sheets are another reason why the RGO–Fe_3O_4 composites exhibit better absorbing abilities.[1] Thirdly, there are dipoles present in Fe_3O_4 especially when their sizes are at the

Table 1 Magnetic properties of Fe_3O_4 NPs and RGO–Fe_3O_4 composites

Sample	M_s (emu g^{-1})	H_c (Oe)	M_r (emu g^{-1})
RGO–Fe_3O_4-1	27.6	114.9	4.8
RGO–Fe_3O_4-2	42.4	108.9	7.4
RGO–Fe_3O_4-3	54.3	103.5	9.0
Fe_3O_4	80.2	42.9	9.5

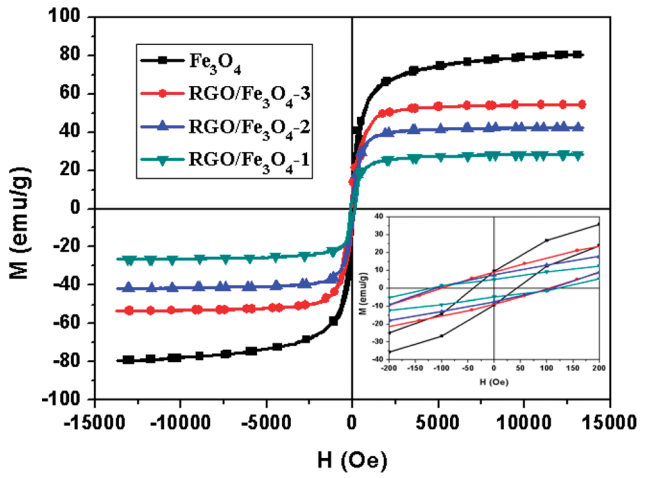

Fig. 7 Magnetization curves of Fe_3O_4 NPs and RGO–Fe_3O_4 composites at room temperature. Inset: the expanded low field magnetization curves.

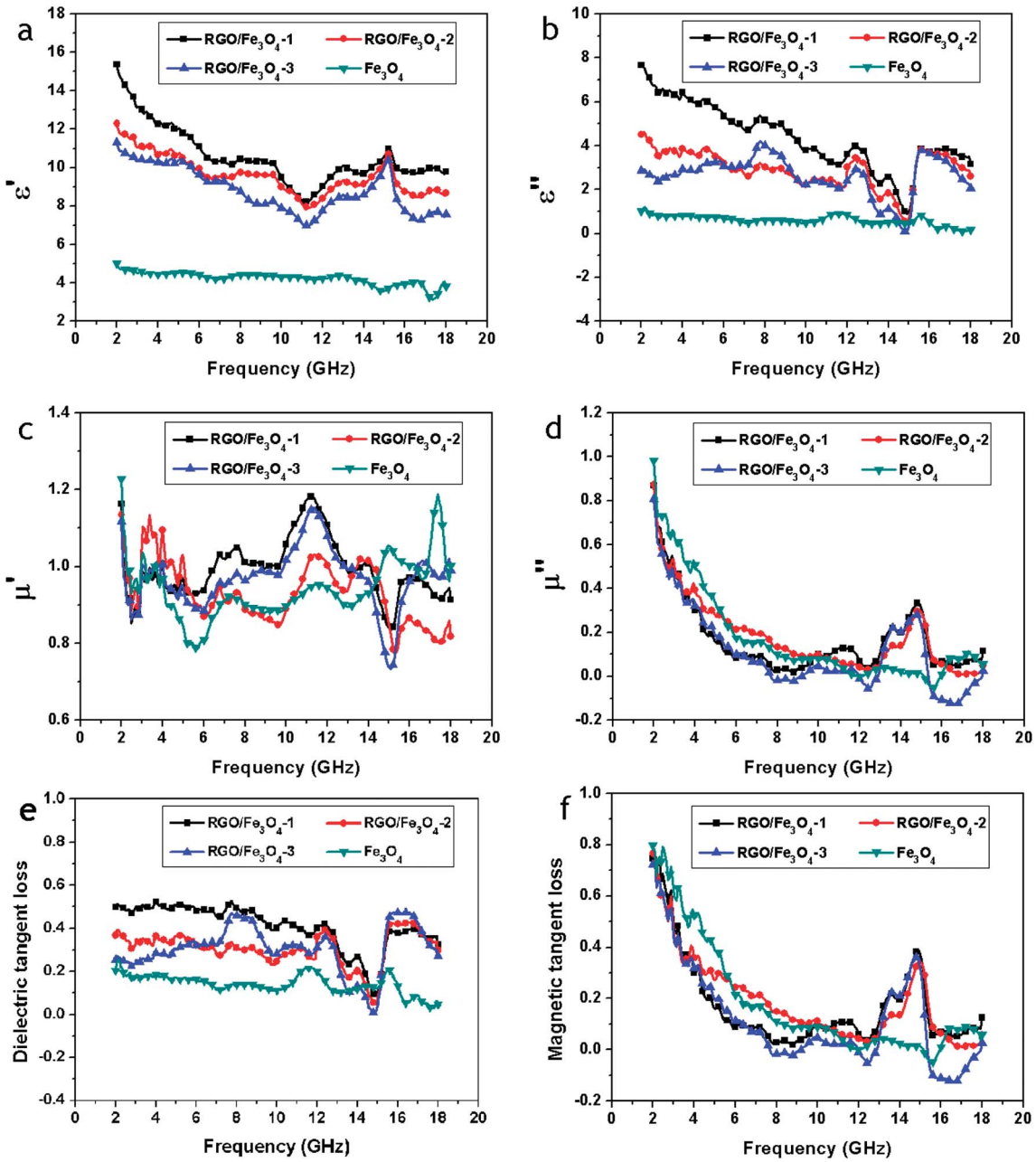

Fig. 8 Frequency dependence on real parts (a) and imaginary parts (b) of the complex permittivity, real parts (c) and imaginary parts (d) of the complex permeability, and the corresponding dielectric loss tangents (e) and magnetic loss tangents (f) of Fe_3O_4 and RGO–Fe_3O_4 composites.

nanoscale. The number of surface atoms with unsaturated bonds greatly increases as the size decreases, causing an increase of the dipoles. Consequently, the dipole polarizations can contribute to the dielectric loss.[4] If we just make a mixture of GO with Fe_3O_4 followed by a reduction, the Fe_3O_4 NPs will conglomerate, then the dipole polarization will weaken. Moreover, the interfaces between the RGO lamella and Fe_3O_4 NPs are clearly observed, as shown in Fig. 1. The interfacial polarization and the associated relaxation contribute to the dielectric loss.[1] This is another reason why the RGO–Fe_3O_4 composites have stronger EM absorption than Fe_3O_4 NPs. Furthermore, according to the free electron theory, $\varepsilon'' = 1/2\varepsilon_0\pi\rho f$, where ε_0 is the permittivity of a vacuum, ρ is the resistivity, f is the frequency of the microwave.[30,46,47] The conductivity of graphene is high and a conducting network is formed, which enables a reduction in resistivity ρ of the composites and the ε'' becomes higher with the increasing content of graphene.[30] The resistivity of the nanocomposite will decrease due to the increase of the (RGO)/(Fe_3O_4) ratios and results in an increase in dielectric loss.[46] In addition, such higher dielectric loss is also related to electron hopping between Fe^{2+} and Fe^{3+} ions in the B sites as the EM wave field is applied, which has been reported previously.[4,46]

We adopt the Debye dielectric relaxation model (Cole–Cole model) to further interpret the mechanisms of the permittivity

dispersion. According to its expression, the relative complex permittivity can be expressed by the following equation,[1,5,47]

$$\varepsilon_r = \varepsilon_\infty + \frac{\varepsilon_s - \varepsilon_\infty}{1 + j2\pi f\tau} = \varepsilon' - j\varepsilon'' \quad (4)$$

where f, ε_s, ε_∞, and τ are frequency, static permittivity, relative dielectric permittivity at the high-frequency limit, and polarization relaxation time, respectively. Thus, ε' and ε'' can be described by

$$\varepsilon' = \varepsilon_\infty + \frac{\varepsilon_s - \varepsilon_\infty}{1 + (2\pi f)^2\tau^2} \quad (5)$$

$$\varepsilon'' = \frac{2\pi f\tau(\varepsilon_s - \varepsilon_\infty)}{1 + (2\pi f)^2\tau^2} \quad (6)$$

According to eqn (2) and (3), the relationship between ε' and ε'' can be deduced,

$$\left(\varepsilon' - \frac{\varepsilon_s + \varepsilon_\infty}{2}\right)^2 + (\varepsilon'')^2 = \left(\frac{\varepsilon_s - \varepsilon_\infty}{2}\right)^2 \quad (7)$$

Thus, the plot of ε' *versus* ε'' would be a single semicircle, generally denoted as the Cole–Cole semicircle. Each semicircle corresponds to one Debye relaxation process. Fig. 9a–c show the ε'–ε'' curves of the RGO–Fe_3O_4 composites.

At least four Cole–Cole semicircles are clearly found in the ε'–ε'' curves of the RGO–Fe_3O_4 composites. This suggests that there are multiple relaxation processes for the RGO–Fe_3O_4 composites, representing the contribution of the Debye relaxation process to the enhanced dielectric properties of the RGO–Fe_3O_4 composites.[1] In the composites, the existence of interfaces gives rise to interfacial polarization or the Maxwell–Wagner effect. This phenomenon appears in heterogeneous media due to the accumulation of charges at the interfaces and the formation of large dipoles on particles or clusters.[47] Evidently, the Cole–Cole semicircle is distorted, suggesting that except for the dielectric relaxation, other mechanisms such as conductance loss, interfacial polarization and oxygen defects may contribute to the permittivity spectra.[45]

It reveals that the value of the magnetic loss (tan δ_M) of the RGO–Fe_3O_4 composites first declines at 2.0–8.0 GHz, remains in the 8.0–12.4 GHz range, and then exhibits broad resonance peaks at 12.4–15.6 GHz with a maximum value at 14.8 GHz, as presented in Fig. 8f. The magnetic loss is related to the eddy current effect and the anisotropy energy of the composites. For the ferromagnetic absorber, the microwave absorption properties are usually subject to degradation caused by the eddy current effect in the high-frequency region. The μ'' can be expressed by[4]

$$\mu'' \approx 2\pi\mu_0(\mu')^2\sigma d^2 f/3 \quad (8)$$

where σ and μ_0 are the electric conductivity and the permeability in vacuum, respectively. Thus, C_0 can be described by

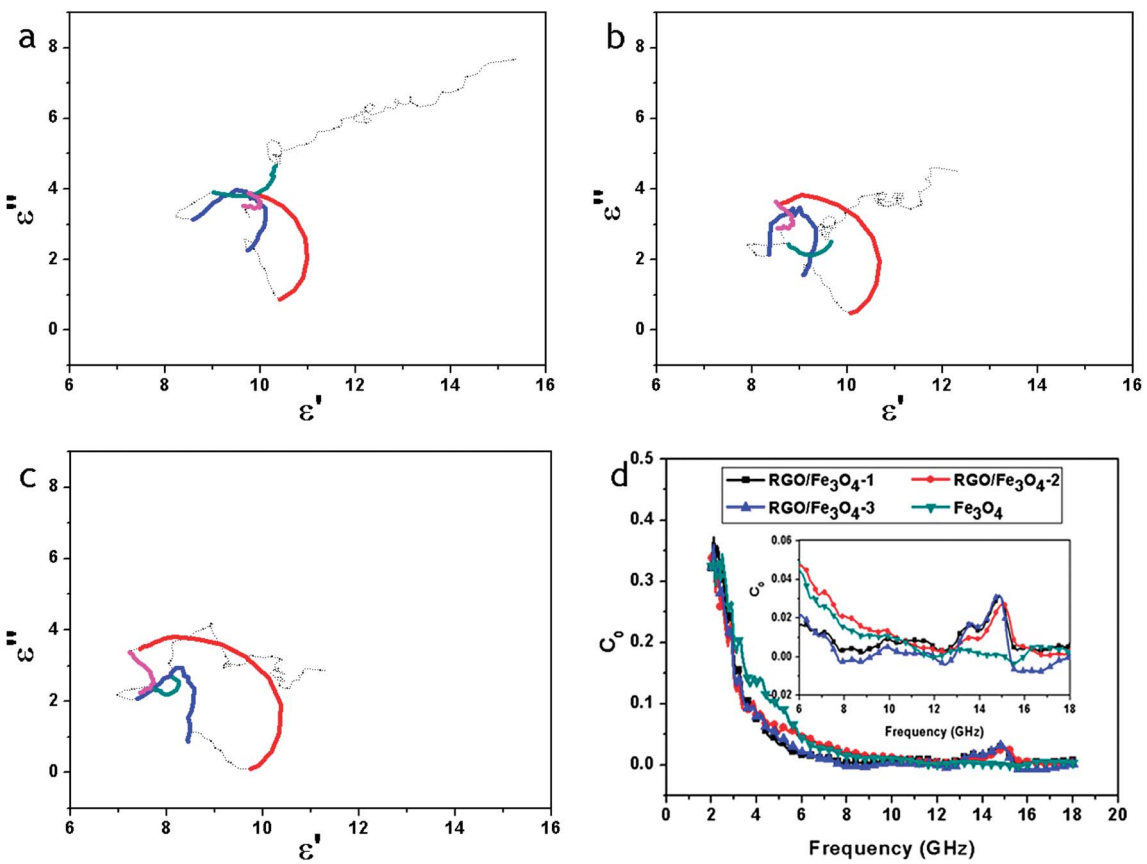

Fig. 9 ε'–ε'' curves of RGO–Fe_3O_4-1 composite (a), RGO–Fe_3O_4-2 composite (b) and RGO–Fe_3O_4-3 composite (c); C_0–f curves of Fe_3O_4 NPs and RGO–Fe_3O_4 composites (d), inset is the expansion of the curves.

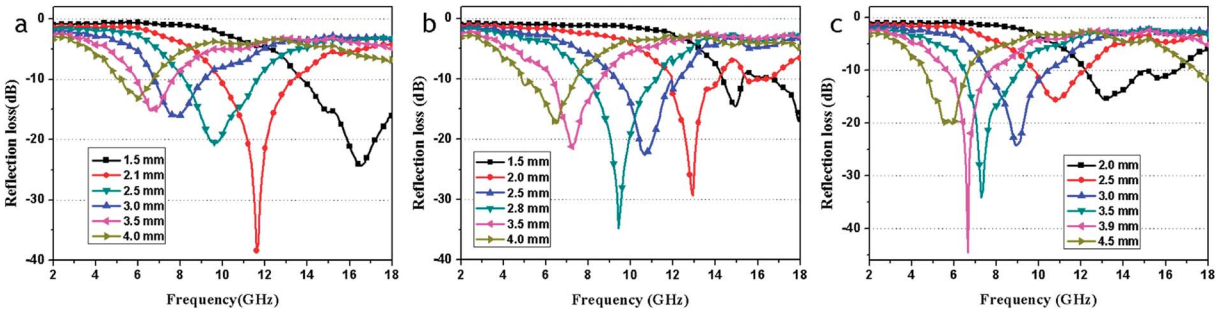

Fig. 10 The calculated reflection losses for RGO-Fe_3O_4-1 (a), RGO-Fe_3O_4-2 (b) and RGO-Fe_3O_4-3 (c) with different thicknesses in the frequency range of 2–18 GHz.

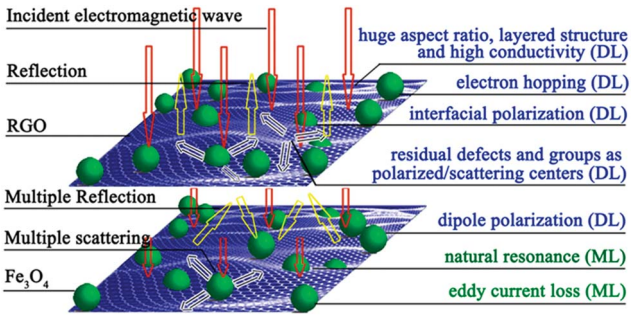

Fig. 11 Schematic of possible microwave absorbing mechanisms of the RGO–Fe_3O_4 composites.

$$C_0 = \mu''(\mu')^{-2}f^{-1} = 2\pi\mu_0\sigma d^2/3 \quad (9)$$

If the magnetic loss results from eddy current loss, the values of C_0 are constant when the frequency is varied.[48]

Fig. 9d shows the C_0–f curves of the pure Fe_3O_4 NPs and the RGO–Fe_3O_4 composites. For the pure Fe_3O_4 NPs, the values of C_0 are almost constant in the high-frequency region (8–18 GHz). However, for the RGO–Fe_3O_4 composites, those values of C_0 exhibit a broad peak in the 12.4–15.6 GHz frequency range. This implies that the pure Fe_3O_4 NPs have a significant eddy current effect in the high-frequency region (8–18 GHz), and the range of eddy current effect will be decreased with the introduction of RGO. Besides, the magnetic loss in the RGO–Fe_3O_4 composites was mainly caused by the natural resonance in the frequency range 2.0–8.0 GHz and 12.4–15.6 GHz and the eddy current effect in the frequency range 8.0–12.4 GHz and 15.6–18.0 GHz.

The natural resonance in the frequency range 2.0–8.0 GHz and 12.4–15.6 GHz can be attributed to the small size effect and the introduction of RGO. According to the natural-resonance equation,[4,49] for ferromagnetic materials,

$$2\pi f_r = rH_a \quad (10)$$

$$H_a = 4|K_1|/3\mu_0 M_s \quad (11)$$

where r is the gyromagnetic ratio, H_a is the anisotropy energy, and $|K_1|$ is the anisotropy coefficient. On one hand, the anisotropy energy of small materials, especially on the nanoscale, would remarkably increase due to the surface anisotropic field by the small size effect.[49,50] On the other hand, the M_s value of the RGO–Fe_3O_4 composites is much lower than that of the pure Fe_3O_4 NPs (Fig. 7), thus the anisotropy energy of the RGO–Fe_3O_4 composites is higher than that of the pure Fe_3O_4 NPs. The higher anisotropy energy is helpful for the improvement of microwave absorption properties.[4]

To further study the microwave absorption properties, the reflection loss (R_L) was calculated by the following equations based on the transmit-line theory:

$$Z_{in} = \sqrt{\frac{\mu_r}{\varepsilon_r}}\tanh\left[j\left(\frac{2\pi fd}{c}\right)\sqrt{\varepsilon_r\mu_r}\right] \quad (12)$$

$$R_L(\mathrm{dB}) = 20\log\left|\frac{Z_{in}-1}{Z_{in}+1}\right| \quad (13)$$

where Z_{in} is the input impedance of the absorber, μ_r and ε_r are respectively the relative complex permeability and permittivity, f is the frequency of microwaves, d is the thickness of the absorber, and c is the velocity of electromagnetic waves in free space. The impedance matching condition is determined by the combination of the six parameters: ε', ε'', μ', μ'', f, and d.[20]

Fig. 10 shows the calculated theoretical reflection loss of the RGO–Fe_3O_4 composites with different thickness in the range of 2–18 GHz. It can be observed that the thickness of the absorbers has a great influence on the microwave absorbing properties. In addition, the maximum R_L absorption gradually appeared to shift toward a lower frequency with the increase of thickness.[1]

As shown in Fig. 10a, the maximum R_L reaches −38.4 dB at 11.6 GHz for the RGO–Fe_3O_4-1 composite with a thickness of only 2.1 mm. With a thickness of 1.5 mm, the maximum R_L which can be achieved is −24.2 dB at 16.6 GHz, and a bandwidth of R_L less than −10 dB (90% absorption[19]) can reach up to 4.2 GHz (from 13.8 to 18.0 GHz). The absorption bandwidth with R_L below −10 dB is up to 12.7 GHz (from 5.3 to 18.0 GHz) with a thickness in the range of 1.5–4.0 mm. For the RGO–Fe_3O_4-2 composite (Fig. 10b), the maximum R_L reaches −34.9 dB at 9.4 GHz with a thickness of only 2.8 mm, and a bandwidth of R_L less than −10 dB can reach up to 3.2 GHz (from 8.0 to 11.2 GHz). Whereas for the RGO–Fe_3O_4-3 composite (Fig. 10c), the maximum R_L even reaches −44.6 dB at 6.6 GHz with a thickness of 3.9 mm, and a bandwidth of R_L less than −10 dB can reach up to 2.0 GHz (from 5.7 to 7.7 GHz). With a thickness of 2.0 mm, the maximum R_L can be achieved at −15.9 dB at 13.2 GHz, and a bandwidth of R_L less than −10 dB

can reach up to 4.3 GHz (from 12.2 to 16.5 GHz). It is observed that for the RGO–Fe_3O_4 composites, the optimal thickness will increase whereas the matching frequency will decrease when the (RGO)/(Fe_3O_4) ratio decreases. As previously stated, we conclude that the as-prepared RGO–Fe_3O_4 composites show an excellent absorption performance in the range of 2–18 GHz and the maximum R_L can be adjusted to a different frequency by controlling the thickness. Our RGO–Fe_3O_4 composites exhibit excellent microwave absorption performance in comparison with pure RGO,[3,30] Fe_3O_4 NPs (Fig. S4†) and RGO composites reported.[12]

The excellent microwave absorbing performance of the RGO–Fe_3O_4 composites is mainly attributed to two key factors: impedance matching and electromagnetic wave attenuation.[30] On one hand, the introduction of Fe_3O_4 NPs has lowered the ε_r of the RGO, and improved the equality of the ε_r and μ_r, which helps to improve the level of impedance matching. On the other hand, the RGO–Fe_3O_4 composites have strong electromagnetic wave attenuation, which is determined by their dielectric loss (DL) and magnetic loss (ML) (discussed in Fig. 8e and f). Besides, the enormous aspect ratio, layered structure, and the existence of residual defects and groups of the RGO–Fe_3O_4 composites could cause multiple reflections, which will further enhance the microwave absorbing ability of the composites.[30,41] In general, the enhanced microwave absorbing performance of the composites is attributed to the compensatory effect of the graphene and Fe_3O_4 NPs.[30] To further give a visual demonstration of the microwave absorbing mechanism as discussed above, a schematic diagram is presented in Fig. 11. From the above, the results demonstrate that the RGO–Fe_3O_4 composites could be used as a microwave absorbing material.

4. Conclusion

In summary, the RGO–Fe_3O_4 composites with an obviously enhanced microwave absorption property have been successfully synthesized by a rational one-pot simplified co-precipitation route, which avoided the usage of an inert gas and any additional chemical agents (such as surfactants). The results show that the Fe_3O_4 NPs are very well dispersed on the surface of the RGO nanosheets. The RGO–Fe_3O_4 composites remarkably improved the electromagnetic performance in comparison with the pure RGO, Fe_3O_4 NPs and RGO composites reported, which is attributed to effective complementarities between the dielectric loss and the magnetic loss. The dielectric loss of the composites can be attributed to natural resonance, Debye dipolar relaxation, electron polarization relaxation, interfacial polarization and the unique layered nanostructures *etc.* The magnetic loss of the RGO–Fe_3O_4 composites is mainly caused by the natural resonance in the frequency range 2.0–8.0 GHz and 12.4–15.6 GHz, and the eddy current effect in the frequency range 8.0–12.4 GHz and 15.6–18.0 GHz. For the RGO–Fe_3O_4-3 composite, the maximum R_L reaches −44.6 dB at 6.6 GHz with a thickness of 3.9 mm, and a bandwidth of R_L less than −10 dB can reach up to 4.3 GHz (from 12.2 to 16.5 GHz) with a thickness of 2.0 mm. Additionally, the microwave absorption property can be tuned easily by varying the (RGO)/(Fe_3O_4) ratio and layer thickness of the samples. It is believed that such composites will find wide applications in microwave absorbing area.

Acknowledgements

This work was supported by the Spaceflight Foundation of China (no. 2011XW110001C110001), the Spaceflight Innovation Foundation of China (no. 2011XT110002C110002) and the Basic Research Foundation of Northwestern Polytechnical University (no. JC201269).

References

1 D. Z. Chen, G. S. Wang, S. He, J. Liu, L. Guo and M. S. Cao, *J. Mater. Chem. A*, 2013, **1**, 5996–6003.
2 J. W. Liu, R. C. Che, H. J. Chen, F. Zhang, F. Xia, Q. S. Wu and M. Wang, *Small*, 2012, **8**, 1214–1221.
3 C. Wang, X. J. Han, P. Xu, X. L. Zhang, Y. C. Du, S. R. Hu, J. Y. Wang and X. H. Wang, *Appl. Phys. Lett.*, 2011, **98**, 072906.
4 C. L. Zhu, M. L. Zhang, Y. J. Qiao, G. Xiao, F. Zhang and Y. J. Chen, *J. Phys. Chem. C*, 2010, **114**, 16229–16235.
5 H. L. Yu, T. S. Wang, B. Wen, M. M. Lu, Z. Xu, C. L. Zhu, Y. J. Chen, X. Y. Xue, C. W. Sun and M. S. Cao, *J. Mater. Chem.*, 2012, **22**, 21679–21685.
6 X. A. Li, B. Zhang, C. H. Ju, X. J. Han, Y. C. Du and P. Xu, *J. Phys. Chem. C*, 2011, **115**, 12350–12357.
7 Y. C. Qing, W. C. Zhou, F. Luo and D. M. Zhu, *Carbon*, 2010, **48**, 4074–4080.
8 X. Bai, Y. H. Zhai and Y. Zhang, *J. Phys. Chem. C*, 2011, **115**, 11673–11677.
9 L. Wang, F. He and Y. Z. Wan, *J. Alloys Compd.*, 2011, **509**, 4726–4730.
10 D. Y. Pan, J. C. Zhang, Z. Li and M. H. Wu, *Adv. Mater.*, 2010, **22**, 734–738.
11 H. X. Chang, G. F. Wang, A. Yang, X. M. Tao, X. Q. Liu, Y. D. Shen and Z. J. Zheng, *Adv. Funct. Mater.*, 2010, **20**, 2893–2902.
12 E. L. Ma, J. J. Li, N. Q. Zhao, E. Z. Liu, C. N. He and C. S. Shi, *Mater. Lett.*, 2013, **91**, 209–212.
13 G. Goncalves, P. A. A. P. Marques, C. M. Granadeiro, H. I. S. Nogueira, M. K. Singh and J. Grácio, *Chem. Mater.*, 2009, **21**, 4796–4802.
14 S. Liu, J. Q. Tian, L. Wang, H. L. Li, Y. W. Zhang and X. P. Sun, *Macromolecules*, 2010, **43**, 10078–10083.
15 G. P. Kim, I. Nam, N. D. Kim, J. Park, S. Park and J. Yi, *Electrochem. Commun.*, 2012, **22**, 93–96.
16 A. Prakash, S. Chandra and D. Bahadur, *Carbon*, 2012, **50**, 4209–4219.
17 Y. Q. Zhan, F. B. Meng, Y. J. Lei, R. Zhao, J. C. Zhong and X. B. Liu, *Mater. Lett.*, 2011, **65**, 1737–1740.
18 Y. Q. Zhan, R. Zhao, Y. J. Lei, F. B. Meng, J. C. Zhong and X. B. Liu, *Appl. Surf. Sci.*, 2011, **257**, 4524–4528.
19 Y. Yang, X. L. Liu, Y. Yang, W. Xiao, Z. W. Li, D. S. Xue, F. S. Li and J. Ding, *J. Mater. Chem. C*, 2013, **1**, 2875–2885.
20 W. C. Zhou, X. J. Hu, X. X. Bai, S. Y. Zhou, C. Y. Sun, J. Yan and P. Chen, *ACS Appl. Mater. Interfaces*, 2011, **3**, 3839–3845.

21 S. H. Liu, R. M. Xing, F. Lu, R. K. Rana and J. J. Zhu, *J. Phys. Chem. C*, 2009, **113**, 21042–21047.
22 J. S. Chen, Y. M. Zhang and D. Lou, *ACS Appl. Mater. Interfaces*, 2011, **3**, 3276–3279.
23 J. Su, M. H. Cao, L. Ren and C. W. Hu, *J. Phys. Chem. C*, 2011, **115**, 14469–14477.
24 W. Hummers, Jr and R. E. Offeman, *J. Am. Chem. Soc.*, 1958, **80**, 1339.
25 M. Z. Kassaee, E. Motamedi and M. Majdi, *Biochem. Eng. J.*, 2011, **172**, 540–549.
26 P. S. Teo, H. N. Lim, N. M. Huang, C. H. Chia and I. Harrison, *Ceram. Int.*, 2012, **38**, 6411–6416.
27 X. P. Shen, J. L. Wu, S. Bai and H. Zhou, *J. Alloys Compd.*, 2010, **506**, 136–140.
28 Y. C. Si and E. T. Samulski, *Chem. Mater.*, 2008, **20**, 6792–6797.
29 H. Wei, W. s. Yang, Q. Xi and X. Chen, *Mater. Lett.*, 2012, **82**, 224–226.
30 X. Sun, J. P. He, G. X. Li, J. Tang, T. Wang, Y. X. Guo and H. R. Xue, *J. Mater. Chem. C*, 2013, **1**, 765–777.
31 G. B. Sun, B. X. Dong, M. H. Cao, B. Q. Wei and C. W. Hu, *Chem. Mater.*, 2011, **23**, 1587–1593.
32 Y. Q. Zhan, F. B. Meng, X. L. Yang, R. Zhao and X. B. Liu, *Mater. Sci. Eng., B*, 2011, **176**, 1333–1339.
33 P. B. Liu, Y. Huang and L. Wang, *Mater. Lett.*, 2013, **91**, 125–128.
34 H. L. Guo, X. F. Wang, Q. Y. Qian, F. B. Wang and X. H. Xia, *ACS Nano*, 2009, **3**, 2653–2659.
35 H. K. Jeong, Y. P. Lee, R. J. W. E. Lahaye, M. H. Park, K. H. An, I. J. Kim, C. W. Yang, C. Y. Park, R. S. Ruoff and Y. H. Lee, *J. Am. Chem. Soc.*, 2008, **130**, 1362–1366.
36 H. P. Cong, X. C. Ren, P. Wang and S. H. Yu, *ACS Nano*, 2012, **6**, 2693–2703.
37 C. Z. Zhu, S. J. Guo, Y. X. Fang and S. J. Dong, *ACS Nano*, 2010, **4**, 2429–2437.
38 L. L. Ren, S. Huang, W. Fan and T. X. Liu, *Appl. Surf. Sci.*, 2011, **258**, 1132–1138.
39 Y. Z. Xue, B. Wu, L. Jiang, Y. L. Guo, L. P. Huang, J. J. Chen, J. H. Tan, D. C. Geng, B. R. Luo, W. P. Hu, G. Yu and Y. Q. Liu, *J. Am. Chem. Soc.*, 2012, **134**, 11060–11063.
40 F. J. Zhang, J. Liu, K. Zhang, W. Zhao, W. K. Jang and W. C. Oh, *Korean J. Chem. Eng.*, 2012, **29**, 989–993.
41 G. M. Rutter, J. N. Crain, N. P. Guisinger, T. Li, P. N. First and J. A. Stroscio, *Science*, 2007, **317**, 219–222.
42 X. B. Fan, W. C. Peng, Y. Li, X. Y. Li, S. L. Wang, G. L. Zhang and F. B. Zhang, *Adv. Mater.*, 2008, **20**, 4490–4493.
43 D. Zhou, T. L. Zhang and B. H. Han, *Microporous Mesoporous Mater.*, 2013, **165**, 234–239.
44 F. He, J. T. Fan, D. Ma, L. M. Zhang, C. Leung and H. L. Chan, *Carbon*, 2010, **48**, 3139–3144.
45 H. J. Wu, L. D. Wang, S. L. Guo, Y. M. Wang and Z. Y. Shen, *Mater. Chem. Phys.*, 2012, **133**, 965–970.
46 Y. J. Chen, G. Xiao, T. S. Wang, Q. Y. Ouyang, L. H. Qi, Y. Ma, P. Gao, C. L. Zhu, M. S. Cao and H. B. Jin, *J. Phys. Chem. C*, 2011, **115**, 13603–13608.
47 S. He, G. S. Wang, C. Lu, J. Liu, B. Wen, H. Liu, L. Guo and M. S. Cao, *J. Mater. Chem. A*, 2013, **1**, 4685–4692.
48 X. F. Zhang, X. L. Dong, H. Huang, Y. Y. Liu, W. N. Wang, X. G. Zhu, B. Lv and J. P. Lei, *Appl. Phys. Lett.*, 2006, **89**, 053115.
49 Y. J. Chen, P. Gao, R. X. Wang, C. L. Zhu, L. J. Wang, M. J. Cao and H. B. Jin, *J. Phys. Chem. C*, 2009, **113**, 10061–10064.
50 D. L. Leslie-Pelecky and R. D. Rieke, *Chem. Mater.*, 1996, **8**, 1770–1783.

